

Acoustic tomography of a coastal front in Haro Strait, British Columbia

P. Elisseff and H. Schmidt

Department of Ocean Engineering, Massachusetts Institute of Technology, Cambridge, Massachusetts 02139

M. Johnson and D. Herold

Applied Ocean Physics and Engineering Department, Woods Hole Oceanographic Institution, Woods Hole, Massachusetts 02543

N. R. Chapman and M. M. McDonald

Centre for Earth and Ocean Research, University of Victoria, Victoria, British Columbia V8W 2Y2, Canada

(Received 24 March 1997; revised 11 February 1999; accepted 6 March 1999)

An experiment validating the concept of acoustically focused oceanographic sampling (AFOS) was recently implemented in Haro Strait, British Columbia (Canada). Four 16-element vertical receiver arrays were moored around the location of a coastal front driven by estuarine and tidal forcing. Various signals were transmitted from array to array and from a moving source to the arrays over a period of five weeks. Tomographic signals were transmitted over a wide frequency band (150 Hz to 15 kHz). The novelty of the Haro Strait data set resides in its unusual tomographic features: ranges are short (less than 3 km), sound speed perturbations are small (2 to 3 m/s), and currents are relatively strong (3.5 kts). Light-bulb-generated wideband acoustic signals are used in this paper in conjunction with local nonacoustic measurements in order to image the three-dimensional sound speed and current fields within the water mass enclosed by the moored arrays. The combined use of integral and local data leads to a significant decrease of the field estimate uncertainty while maintaining a coverage of the area not achievable by nonacoustic means. © 1999 Acoustical Society of America. [S0001-4966(99)00307-0]

PACS numbers: 43.30.Pc, 43.60.Rw [SAC-B]

INTRODUCTION

Ocean acoustic tomography was suggested two decades ago as a means of performing large-scale measurement of oceanographic quantities such as temperature and current in deep ocean.¹ Its feasibility has since been repeatedly demonstrated.²⁻⁷ A number of studies have been made in order to adapt deep ocean methods to coastal environments, in which shallow water propagation and high environmental variability make the inversion significantly more difficult.⁸⁻¹¹ While coastal tomography remains a topic of active research, recent developments in wireless communication technology combined with significant increases in computing power have opened the way to acoustically focused oceanographic sampling (AFOS).¹² The AFOS consists of a network of acoustic arrays connected to a fleet of autonomous underwater vehicles (AUV) and to a shore station using wireless local area network technology. Nonacoustic moorings may be integrated in the network as additional nodes when available. A real-time field estimate of temperature or current in the region of interest is computed by combining the various integral and local data sets available. Integral, synoptic data is provided by the acoustic tomographic inversion while nonacoustic sensors yield local point measurements. The real-time field estimate and its associated error field are then used to adaptively direct AUVs towards regions where high resolution is required due to large gradi-

ents or large uncertainties. The AFOS provides *rapid environmental assessment*, which is important for coastal oceanography and operation of naval systems.

In this context a feasibility experiment was recently performed in Haro Strait, British Columbia.¹³ Its first objective was to test the available technology when integrated into a single network. Its second objective was to demonstrate the scientific relevance of AFOS by investigating mixing mechanisms in the highly active Haro Strait region. Four 16-element vertical receiver arrays were moored south of Stuart Island around the location of a coastal front driven by estuarine and tidal forcing (see Fig. 1). Four nonacoustic moorings were located around the acoustic network, measuring local current, temperature, and salinity. An extensive and varied acoustic data set was generated in the course of five weeks (June–July 1996). Tomographic signals were transmitted over a wide frequency band (150 Hz to 15 kHz). The novelty of the Haro Strait data set resides in its unusual tomographic features: ranges are short (less than 3 km), sound speed perturbations are small (2–3 m/s), and currents are relatively strong (up to 5 kts). Operational constraints place stringent demands on the oceanic field estimate provided by AFOS. Its computational load must be light enough, namely of the order of a few minutes at most. The inversion must be able to withstand large environmental uncertainties as well as accommodate a wide variety of data sets. In order to satisfy the robustness constraint, classical deep ocean travel time tomography and oceanographic data assimilation tech-

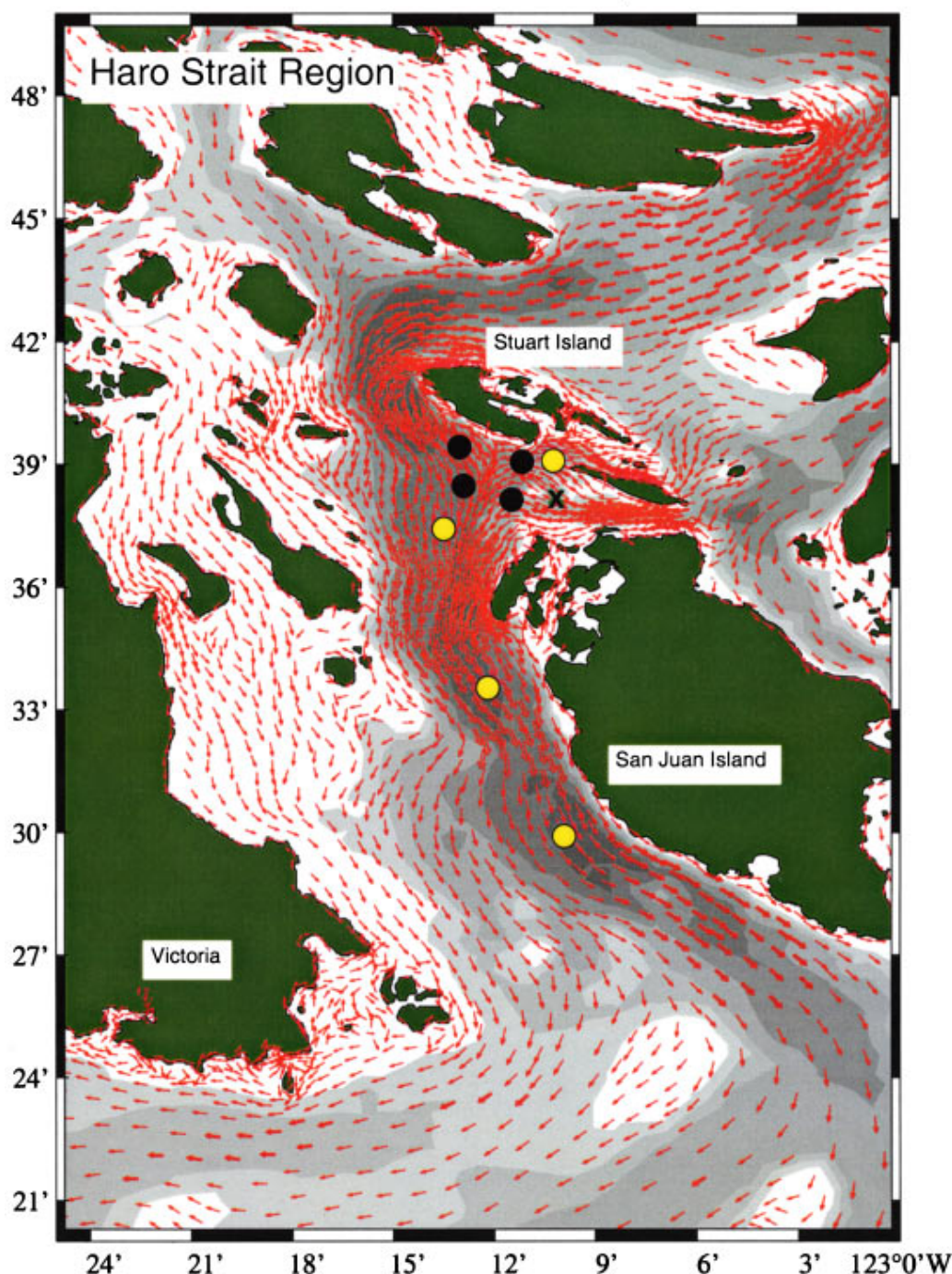


FIG. 1. Topographic map of the Haro Strait region with predicted ebb tide currents during the experiment. Tomographic arrays (black circles) were deployed to investigate the front south of Stuart island. Current meter moorings (yellow circles) and a meteorological surface buoy (black cross) will help clarify the larger-scale circulation (courtesy of R. Pawlowicz, IOS).

niques are combined in this paper and adapted to the Haro Strait environment. While these techniques are not new in themselves, the combined use of interdisciplinary models and data sets in the context of coastal ocean imaging raises several issues as of yet unresolved. Resolution and parameter sensitivity of the various models, for instance, have been shown to be critical factors in successfully coupling oceanographic and acoustic models.¹⁴ The possible gains from jointly extracting environmental information from integral and local data sets, while heuristically and qualitatively

clear, are still hardly quantified. Furthermore, the integration of synoptic acoustic estimates with nonacoustic data sets and models in coastal environments remains a topic of active research.^{15,16}

Far from exhaustively answering the above issues, this paper proposes to explore the analytical and quantitative aspects involved in the combination of multiple data sets, both integral and local, in the operational setting of the Haro Strait experiment. The experimental configuration is described in the next section. The combined inversion formalism is devel-

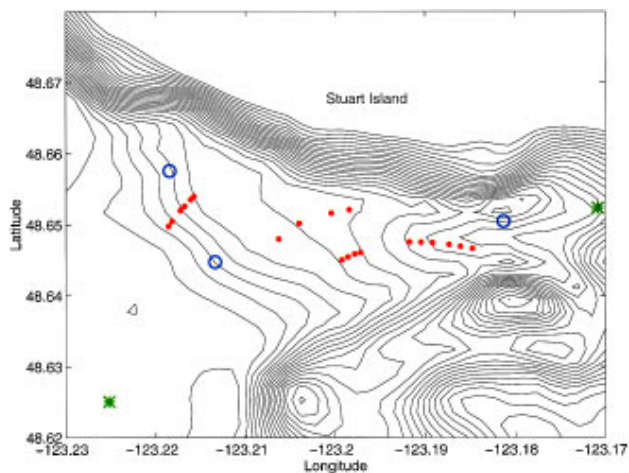


FIG. 2. Bathymetric map of the experimental site. Contours are 10 m apart. Blue circles: WHOI receiver arrays. Green stars: IOS moorings. Red dots: source locations.

oped in the following section. Numerical results, including synthetic data as well as Haro Strait data, are presented in Sec. III.

I. BACKGROUND

A. Experimental configuration

Four vertical acoustic line arrays (hereafter called WHOI moorings) were initially deployed south of Stuart island (see Figs. 1 and 2). The southeastern mooring, located near Danger Shoal, was lost at an early stage of the experiment because of unexpectedly strong tidal currents. Each mooring consisted of 16 receivers, a 1.5-kHz tomographic source, and a 15-kHz communication source (see Fig. 3). A chain of thermistors was added to moorings NW and NE. The acoustic data acquired on each receiver array were sent back to shore via a surface radio link at a rate of 35 kbauds.

Four nonacoustic moorings (hereafter referred to as IOS moorings) were deployed along the Haro Strait channel (see Fig. 1). Local temperature, salinity, current magnitude, and current direction were recorded by these moorings at discrete depths. Only the two IOS moorings closest to the network of

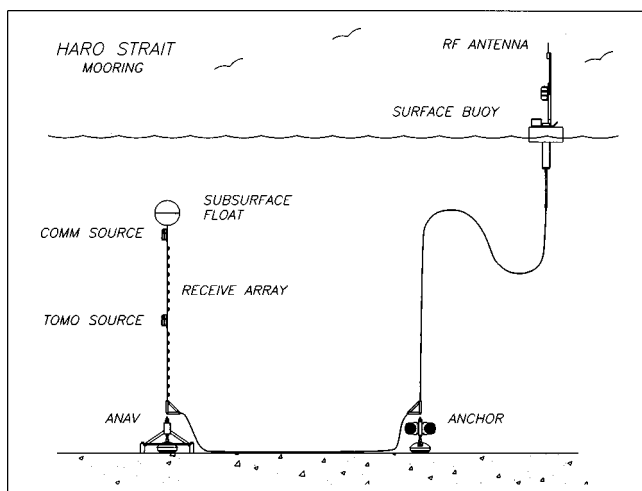


FIG. 3. Haro Strait mooring design.

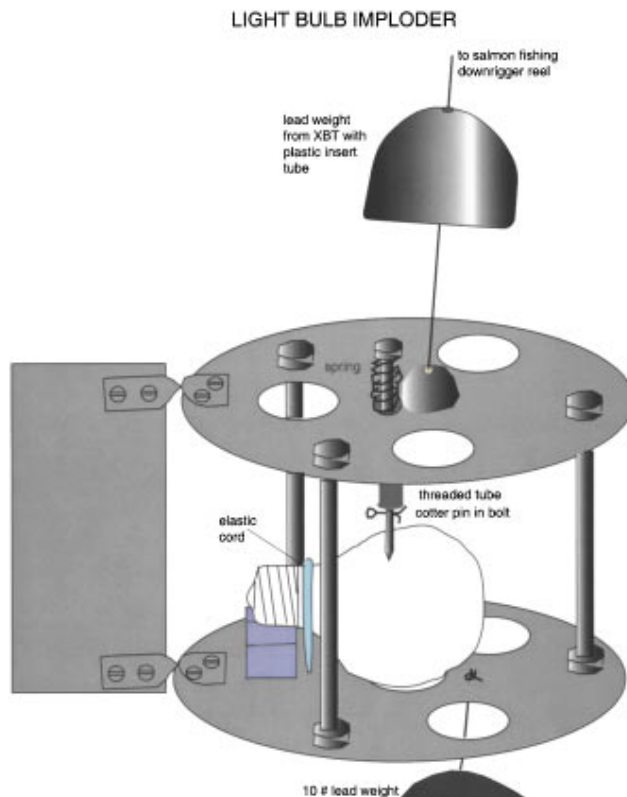


FIG. 4. Source design.

acoustic arrays are used in this analysis. The IOS mooring sensors were located at a depth of 25, 70 (SW only), and 120 m. During the 2-h time period studied in this paper, current magnitudes of up to 3.5 kts and temperatures variations of up to 1.5 °C were observed.

The moving source used in this paper consisted of ship-deployed light bulbs. Source locations were obtained using differential Global Positioning System (GPS) data, and the locations corresponding to the shots used in this paper are shown in Fig. 2. These shots were recorded on all three moorings, and were all deployed within a time period of approximately 90 mins. Source depths ranged from 30 to 70 m. Source levels were approximately 160 to 170 dB/1 μ Pa. The light bulbs were lowered to a specified depth in the casing apparatus shown in Fig. 4. The shot was then triggered by breaking the bulb at depth using an operator-released lead mass that dropped along the cable from the ship to the casing. Light bulbs generate a short reproducible bubble pulse waveform whose spectral peak is typically about 500 Hz at a depth of 50 m, with a 3-dB bandwidth of approximately 300 Hz. Although there is significant spectral content to several kHz, the band was limited in this experiment by the relatively low sampling frequency of 1750 Hz. An example of the raw acoustic signal from one of the light bulbs is shown in Fig. 5.

B. Data conditioning

Individual acoustic time series were match filtered using a single arrival as a substitute for the actual source signal. Absolute timing was provided by the acoustic acquisition system.¹⁷ The magnitude of the matched filter output was

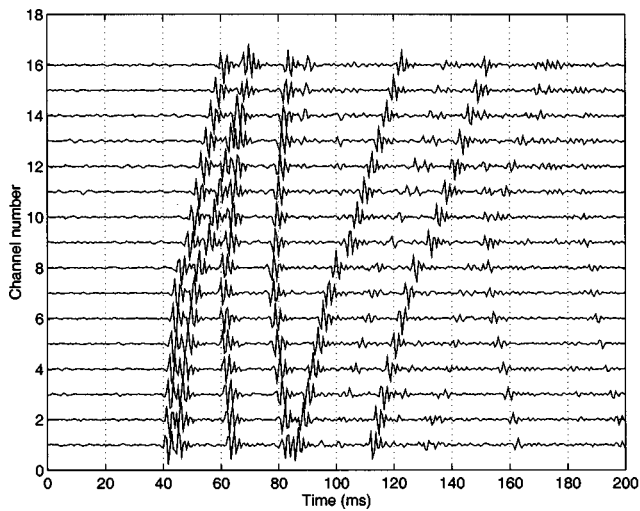


FIG. 5. Raw time series: shot 32, 20 June 1996 02:43 GMT, SW WHOI mooring.

then low-pass filtered using a zero-phase third-order Butterworth filter with a cutoff frequency of 500 Hz. Direct and surface ray arrival times were subsequently measured by identification of the corresponding local maxima of the filtered time series (see Fig. 6). Acoustic sensor localization was carried out by minimizing the mean square difference between the measured arrival times and the arrival times predicted using the sensor model described in Sec. II A.

Raw temperature, salinity, and current time series were measured by the IOS moorings at a frequency of 12 samples per hour. Temperature and salinity were converted to sound speed using Mackenzie's formula.¹⁸ Individual samples were grouped by 50-min bins and averaged. Standard deviations were found to be between 6 and 13 cm/s for the current field, and 1 and 25 cm/s for the sound speed field.

II. ANALYSIS

In order to combine heterogeneous data sets, a variety of observation models is required. Acoustic sensor displacements are accounted for by a sensor model. This model re-

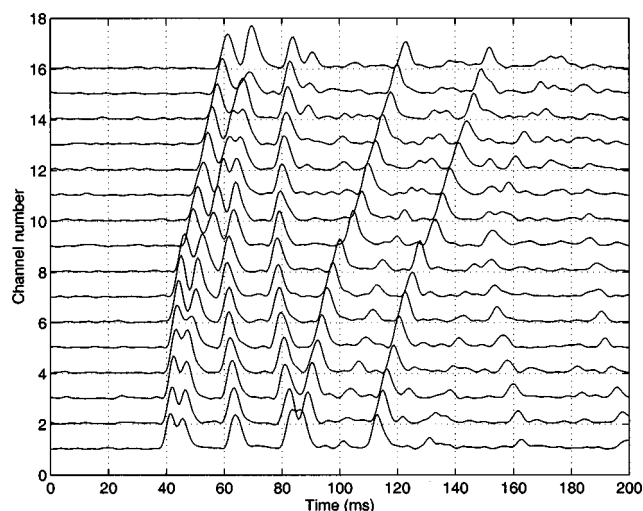


FIG. 6. Filtered time series: shot 32, 20 June 1996 02:43 GMT, SW WHOI mooring.

lates acoustic sensor displacements to array design parameters and local current magnitude at the array. The current model provides predictions of the tidal current field at any point in the observed region. The acoustic model relates sound speed to acoustic travel times. Statistical field estimates provide *a priori* information on the actual field estimates. *A posteriori* current information is provided by local current measurements and acoustic sensor displacements. *A posteriori* sound speed information is provided by local sound speed measurements and acoustic tomographic data. In a first stage an estimate of the current field is computed by objective analysis of the available current data.¹⁹ The current estimate is then externally melded with the tidal current model prediction following a standard data assimilation procedure. The sound speed field is then objectively analyzed using range-averaged acoustic tomographic estimates and local nonacoustic data.

A. Observation models

1. Sensor model

The horizontal displacements of a moored line array placed in a uniform flow can be expressed as²⁰

$$\delta \mathbf{r} = a \left[z - b \ln \left(1 - \frac{z}{c} \right) \right] \boldsymbol{\nu} = af(z) \boldsymbol{\nu} \quad (1)$$

where $\boldsymbol{\nu}$ is a unit vector in the direction of the flow,

$$a = \frac{d}{w}, \quad (2)$$

$$b = \frac{D}{d} - \frac{W}{w}, \quad (3)$$

$$c = \frac{W}{w} + L, \quad (4)$$

d is the cable drag per unit length, w is the cable weight per unit length, D is the drag of the subsurface buoy, W is the buoyancy of the subsurface buoy, and L is the total length of the cable. The coefficients b and c are true constants which depend on the design of a given array. The coefficient a depends quadratically on current magnitude and may be more conveniently expressed as $a = \alpha U^2$, where U is the current magnitude at the location of the array. An acoustic transmission in the horizontal direction \mathbf{p} will then be affected by the projection δR of the array displacements in that direction:

$$\delta R = af(z)(\boldsymbol{\nu}^T \mathbf{p}). \quad (5)$$

Let us now assume the uniform current \mathbf{U} at the array can be decomposed into a reference state $U_o \boldsymbol{\nu}$ and a perturbation \mathbf{u}' . Let us further assume the term $\boldsymbol{\nu}^T \mathbf{p}$ is included in a . The coefficient a can then be expressed as

$$a = a_o + a' = a_o + 2\alpha U_o(\boldsymbol{\nu}^T \mathbf{p})\boldsymbol{\nu}^T \mathbf{u}', \quad (6)$$

where the subscript o refers to the reference state and second-order terms have been neglected. In the case of short-range transmissions, an acoustic estimate \tilde{a} of a' can be easily computed by minimizing the mean square error between measured ray arrival times at the array and their the-

oretical value using an adequate sound speed profile (uniform or historical average) and a reference current vector $U_o \mathbf{v}$. The measured array shape perturbation can be written as

$$\tilde{\mathbf{a}} = 2\alpha(\mathbf{v}^T \mathbf{p}) \mathbf{v}^T \mathbf{u}' + \mathbf{n}_a, \quad (7)$$

where the noise term \mathbf{n}_a is assumed to be Gaussian. Equation (7) establishes a direct linear relationship between the measured value $\tilde{\mathbf{a}}$ and the current perturbation \mathbf{u}' at the array.

2. Current model

An accurate three-dimensional, baroclinic (depth-dependent) finite-element model of tidal currents in the Haro Strait region was recently developed by Foreman *et al.*²¹ In order to decrease the computational load involved in predicting local currents, a two-dimensional, barotropic (depth-independent) version of Foreman's model is used in this paper. The latter model is able to properly account for 90% of the tidal flow variance at the SW IOS mooring and 72% at the NE IOS mooring in Haro Strait. For the purpose of this analysis, Foreman's model can be summarized as

$$\mathbf{U}_o = g(\mathbf{r}, t), \quad (8)$$

where \mathbf{U}_o is the predicted tidal current at the location \mathbf{r} at the time t . The predicted field is used throughout the analysis as the background field. The current perturbation $\tilde{\mathbf{u}}$ measured by the IOS current meters can be related to the true value \mathbf{u}' as

$$\tilde{\mathbf{u}} = \mathbf{u}' + \mathbf{n}_{u,cm}, \quad (9)$$

where the measurement noise vector $\mathbf{n}_{u,cm}$ is assumed to be Gaussian.

3. Acoustic model

For a given source–receiver geometry acoustic travel times perturbations τ can be related to sound speed perturbations by the following linear expression:⁷

$$\tau = \mathbf{E} \mathbf{c}' + \mathbf{n}_{u,a}, \quad (10)$$

where the noise vector $\mathbf{n}_{u,a}$ is assumed to be Gaussian of covariance matrix $\mathbf{R}_{nn}^{(a)}$. In order to reduce the number of degrees of freedom of the original inverse problem the range-independent sound speed perturbation $\delta c(z)$ is decomposed using an arbitrary set of orthogonal functions:

$$\delta c(z) = \phi(z)^T \mathbf{c}'. \quad (11)$$

In the present paper the functions $\phi_j(z)$ are assumed to be “gate” functions, set to zero everywhere except within a specified depth interval $[z_j, z_{j+1}]$ where it is set to unity. These depth intervals are nonoverlapping and cover the entire water column (from 0 to 200 m). The matrix \mathbf{E} can then be expressed as

$$[\mathbf{E}]_{ij} = - \int_{\text{ray}\#i} \frac{\phi_j(z_i)}{c_o^2(r_i, z_i)} ds_i, \quad (12)$$

where c_o is the background sound speed profile. The range r_i and depth z_i along the i th ray are an implicit function of the ray curvilinear abscissa s_i .

B. Inversion formalism

1. Current inversion

Three types of information can be combined in the estimation of the current field: point measurements of current at the two IOS moorings, array shape acoustic estimates at the three WHOI moorings, and *a priori* predictions by Foreman's model. The available point measurements of current can be consolidated through Eq. (9) as

$$\begin{bmatrix} \tilde{\mathbf{u}}_{x,cm} \\ \tilde{\mathbf{u}}_{y,cm} \end{bmatrix} = \begin{bmatrix} \mathbf{I} & \mathbf{O} \\ \mathbf{O} & \mathbf{I} \end{bmatrix} \begin{bmatrix} \mathbf{u}'_{x,cm} \\ \mathbf{u}'_{y,cm} \end{bmatrix} + \begin{bmatrix} \mathbf{n}_{x,cm} \\ \mathbf{n}_{y,cm} \end{bmatrix}, \quad (13)$$

where the x subscript refers to the east/west direction and the y subscript refers to the north/south direction. Similarly, the array shape data can be consolidated using Eq. (7) as

$$\tilde{\mathbf{a}} = [\mathbf{H}_1 \quad \mathbf{H}_2] \begin{bmatrix} \mathbf{u}'_{x,a} \\ \mathbf{u}'_{y,a} \end{bmatrix} + \mathbf{n}_a. \quad (14)$$

The matrices \mathbf{H}_1 and \mathbf{H}_2 are both diagonal and

$$[\mathbf{H}_1]_{jj} = 2\alpha_j(\mathbf{v}_j^T \mathbf{p}_j) \nu_{j,x}, \quad (15)$$

$$[\mathbf{H}_2]_{jj} = 2\alpha_j(\mathbf{v}_j^T \mathbf{p}_j) \nu_{j,y}. \quad (16)$$

The term α_j corresponds to the shape factor α of the acoustic array involved in the j th transmission. Combining (13) and (14) leads to the global observation model of the current field:

$$\begin{bmatrix} \tilde{\mathbf{u}}_{x,cm} \\ \tilde{\mathbf{u}}_{y,cm} \\ \tilde{\mathbf{a}} \end{bmatrix} = \begin{bmatrix} \mathbf{I} & \mathbf{O} & \mathbf{O} & \mathbf{O} & \mathbf{O} & \mathbf{O} \\ \mathbf{O} & \mathbf{O} & \mathbf{O} & \mathbf{I} & \mathbf{O} & \mathbf{O} \\ \mathbf{O} & \mathbf{H}_1 & \mathbf{O} & \mathbf{O} & \mathbf{H}_2 & \mathbf{O} \end{bmatrix} \begin{bmatrix} \mathbf{u}'_{x,cm} \\ \mathbf{u}'_{x,a} \\ \mathbf{u}'_{x,i} \\ \mathbf{u}'_{y,cm} \\ \mathbf{u}'_{y,a} \\ \mathbf{u}'_{y,i} \end{bmatrix} + \begin{bmatrix} \mathbf{n}_{x,cm} \\ \mathbf{n}_{y,cm} \\ \mathbf{n}_a \end{bmatrix}, \quad (17)$$

where $\mathbf{u}'_{x,i}$ and $\mathbf{u}'_{y,i}$ represent the current field perturbation interpolated at the nodes of a specified grid. Equation (17) can be recast in a more compact format as

$$\tilde{\mathbf{u}} = \mathbf{H} \mathbf{u}' + \mathbf{n}_u. \quad (18)$$

The covariances matrices \mathbf{R}_{uu} of $\tilde{\mathbf{u}}$ and \mathbf{R}_{nn} of \mathbf{n}_u can be computed using the space–time correlation function of the current field (see the Appendix). The empirical estimation of this correlation function is discussed in the next section. Equation (18) can then be inverted as^{22,7}

$$\hat{\mathbf{u}}' = \mathbf{K}_u \tilde{\mathbf{u}}, \quad (19)$$

where the gain matrix \mathbf{K}_u is given by

$$\mathbf{K}_u = \mathbf{R}_{uu} \mathbf{H}^T (\mathbf{H} \mathbf{R}_{uu} \mathbf{H}^T + \mathbf{R}_{nn})^{-1}. \quad (20)$$

The associated error covariance matrix of the current perturbation estimate is⁷

$$\mathbf{P}_u = (\mathbf{I} - \mathbf{K}_u \mathbf{H}) \mathbf{R}_{uu}. \quad (21)$$

This concludes the first stage (objective analysis) of the current data assimilation procedure.

The current perturbation estimate \mathbf{u}' can then be merged with the model prediction using the following melding

scheme. The final field estimate at a given node \mathbf{r} for a given component is assumed to be a linear combination of the predicted field and the measured field:¹⁶

$$\hat{U}(\mathbf{r}) = (1 - \lambda(\mathbf{r}))U_o(\mathbf{r}) + \lambda(\mathbf{r})(U_o(\mathbf{r}) + \hat{u}'(\mathbf{r})). \quad (22)$$

The north/south and east/west components are melded independently of each other. Based on the statistical properties of the model and measurement errors a minimum variance estimate of λ can be derived:¹⁶

$$\lambda_{MV}(\mathbf{r}) = \frac{\sigma_m^2(\mathbf{r}) - \rho(\mathbf{r})\sigma_m(\mathbf{r})\sigma_d(\mathbf{r})}{\sigma_m^2(\mathbf{r}) + \sigma_d^2(\mathbf{r}) - 2\rho(\mathbf{r})\sigma_m(\mathbf{r})\sigma_d(\mathbf{r})}, \quad (23)$$

where $\sigma_m(\mathbf{r})$ is the estimated error of the model prediction $U_o(\mathbf{r})$, $\sigma_d(\mathbf{r})$ is the error of the data-based perturbation estimate $\hat{u}'(\mathbf{r})$, and $\rho(\mathbf{r})$ is the correlation between the two. The measurement error $\sigma_d(\mathbf{r})$ is given by the relevant diagonal term of \mathbf{P}_u in Eq. (21). In the absence of an accurate error model of the current prediction made by Foreman's model, the optimal interpolation scheme used by the Harvard Ocean Prediction System is adopted:²³

$$\lambda_{OI}(\mathbf{r}) = \frac{\sigma_{\max} - \sigma_d(\mathbf{r})}{\sigma_{\max} - \sigma_{\min}}, \quad (24)$$

where σ_{\min} and σ_{\max} are the minimum and maximum values of $\sigma_d(\mathbf{r})$. The melded estimate is therefore equal to the model prediction at points where the measurement error is maximal, and is set equal to the measured estimate at point where the measurement error is minimal. The robustness of this melding scheme was demonstrated in several oceanographic data assimilation experiments.²³

2. Sound speed inversion

Two types of information can be combined in the estimation of the sound speed field: point measurements of sound speed at the two IOS moorings and acoustic travel times measured at the three WHOI moorings. This is done in two stages: first the acoustic travel times are used to estimate range-averaged sound speed profiles and their error covariance along the available transmission tracks. These sound speed profiles are then merged with the point measurements and interpolated in order to yield an estimate of the sound speed field.

The covariance matrix $\mathbf{R}_{cc}^{(a)}$ of the sound speed perturbation in Eq. (10) can be estimated using the space-time correlation function of the sound speed field (see the Appendix). The empirical estimation of this correlation function is discussed in the next section. Equation (10) can then be inverted as⁷

$$\hat{\mathbf{c}}' = \mathbf{K}_c^{(a)} \boldsymbol{\tau}, \quad (25)$$

where the gain matrix $\mathbf{K}_c^{(a)}$ is given by

$$\mathbf{K}_c^{(a)} = \mathbf{R}_{cc}^{(a)} \mathbf{E}^T (\mathbf{E} \mathbf{R}_{cc}^{(a)} \mathbf{E}^T + \mathbf{R}_{nn}^{(a)})^{-1}. \quad (26)$$

The associated error covariance matrix of the range-averaged sound speed estimate is⁷

$$\mathbf{P}_c^{(a)} = (\mathbf{I} - \mathbf{K}_c^{(a)} \mathbf{E}) \mathbf{R}_{cc}^{(a)}. \quad (27)$$

The range-averaged sound speed estimate at a given depth z_o can be expressed as

$$\hat{c}'(z_o) = \int_0^1 \beta(\mathbf{r}_{\text{src}}, \mathbf{r}_{\text{rcv}}, z_o, \eta) c'(\mathbf{r}_{\text{src}} + \eta(\mathbf{r}_{\text{rcv}} - \mathbf{r}_{\text{src}})) d\eta, \quad (28)$$

where \mathbf{r}_{src} and \mathbf{r}_{rcv} are the source and receiver locations and c' is the true sound speed perturbation. The weighting or ray sampling function β is given by

$$\beta(\mathbf{r}_{\text{src}}, \mathbf{r}_{\text{rcv}}, z_o, \eta) = \beta_o \sum_i \frac{\phi_j(z_i)}{\cos \theta_i}, \quad (29)$$

where β_o is a normalization factor such that $\beta(\eta)$ integrates to one between 0 and 1. The term ϕ_j is the orthogonal function of Eq. (12) corresponding to the depth bin z_o . The sum is performed over all rays joining the source and the array of receivers. The local ray depth z_i and the local ray grazing angle θ_i are implicit functions of η . The weighting function β is equal to 1 for a source and a receiver located at the same depth in the absence of boundary interaction. The acoustic profile estimates of several transmissions can be consolidated for a given depth as

$$\tilde{\mathbf{c}}_a = \mathbf{F} \mathbf{c}'_i + \mathbf{n}_{c,a}, \quad (30)$$

where \mathbf{c}'_i is the interpolated sound speed field on a specified grid and $\mathbf{n}_{c,a}$ represents additive Gaussian noise. The matrix \mathbf{F} is given by

$$[\mathbf{F}]_{kj} = \beta(\mathbf{r}_{\text{src}}^{(k)}, \mathbf{r}_{\text{rcv}}^{(k)}, z_o, \eta_j^{(k)}) \Delta \eta_j^{(k)}, \quad (31)$$

where $\mathbf{r}_{\text{src}}^{(k)}$ and $\mathbf{r}_{\text{rcv}}^{(k)}$ are the end points of the k th transmission, $\eta_j^{(k)}$ is the local nondimensional range corresponding to the j th node of the global interpolated grid \mathbf{c}_i , and $\Delta \eta_j^{(k)}$ is the nondimensional length of the j th cell intercepted by the ray considered.

Similarly to what was done for the current data, the sound speed perturbation $\tilde{\mathbf{c}}$ measured by the IOS moorings at various times can be related to the true perturbation \mathbf{c}' as

$$\tilde{\mathbf{c}}_{cm} = \mathbf{c}'_{cm} + \mathbf{n}_{c,cm}, \quad (32)$$

where the measurement noise vector $\mathbf{n}_{c,cm}$ is assumed to be Gaussian. Equations (30) and (32) can be combined to yield

$$\begin{bmatrix} \tilde{\mathbf{c}}_{cm} \\ \tilde{\mathbf{c}}_a \end{bmatrix} = \begin{bmatrix} \mathbf{I} & \mathbf{O} \\ \mathbf{O} & \mathbf{F} \end{bmatrix} \begin{bmatrix} \mathbf{c}'_{cm} \\ \mathbf{c}'_i \end{bmatrix} + \begin{bmatrix} \mathbf{n}_{c,cm} \\ \mathbf{n}_{c,a} \end{bmatrix}, \quad (33)$$

which can, in turn, be recast in the more compact form

$$\tilde{\mathbf{c}} = \mathbf{G} \mathbf{c}' + \mathbf{n}_c. \quad (34)$$

Equation (34) can be inverted using the method outlined for Eq. (18). Particular attention must be paid to the covariance matrix of $\tilde{\mathbf{c}}$. As pointed out by Cornuelle and Worcester, the covariance matrix of acoustic sound speed estimates is often nondiagonal and significant errors can be induced by neglecting covariance terms.²⁴ The present method allows these covariance terms to be taken into account by simply inserting the relevant terms of $\mathbf{P}_c^{(a)}$ [Eq. (27)] into the covariance matrix of $\tilde{\mathbf{c}}$ (see the Appendix). In the case of the Haro Strait data set, the absence of a known source transmission time made it necessary to include a global acoustic sound speed

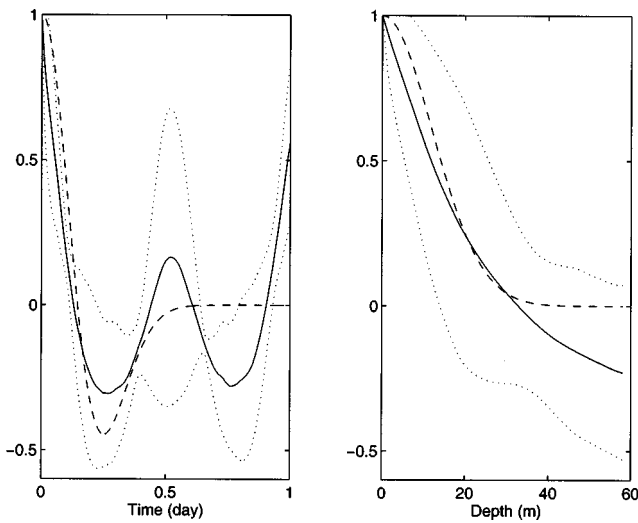


FIG. 7. Sound speed correlation function. Left panel: temporal correlation (IOS mooring data). Right panel: correlation in depth (CTD data). Solid line: average measured correlation. Dotted line: 95% confidence interval. Dashed line: modeled correlation ($T_c = 3.5$ h, $L_z = 12$ m).

offset (single scalar variable) in the model vector \mathbf{c}' in Eq. (34), as only sound speed differences across depths and tracks could be acoustically resolved.

C. Correlation functions

The sound speed and current field perturbations were assumed to be stationary in time and space. The temporal correlations were estimated using the current and sound speed time series measured at the IOS moorings (see Figs. 7 and 8). Figure 8 shows two types of correlations: the correlation measured in the main direction of the flow, i.e., north/south at the IOS SW mooring and east/west at the IOS NE mooring, is smooth and has a relatively broad peak. The correlation measured across the flow has a narrow peak and denotes the presence of turbulence. Inasmuch as this turbu-

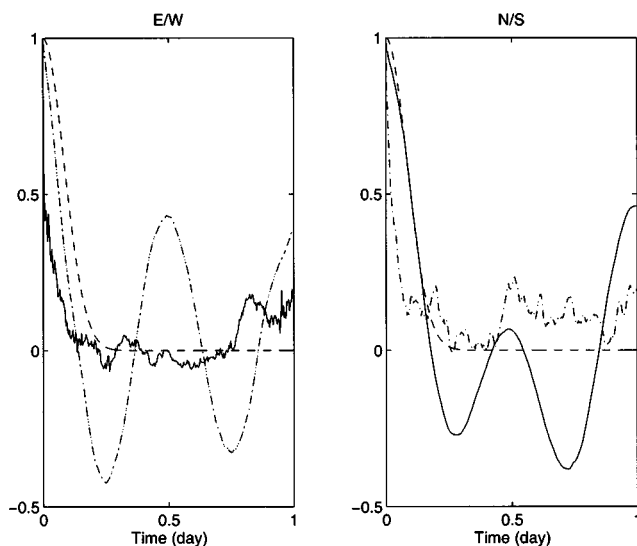


FIG. 8. Current temporal correlation function. Left panel: east/west component. Right panel: north/south component. Solid line: IOS SW mooring. Dash-dotted line: IOS NE mooring. Dashed line: modeled correlation ($T_u = 2$ h).

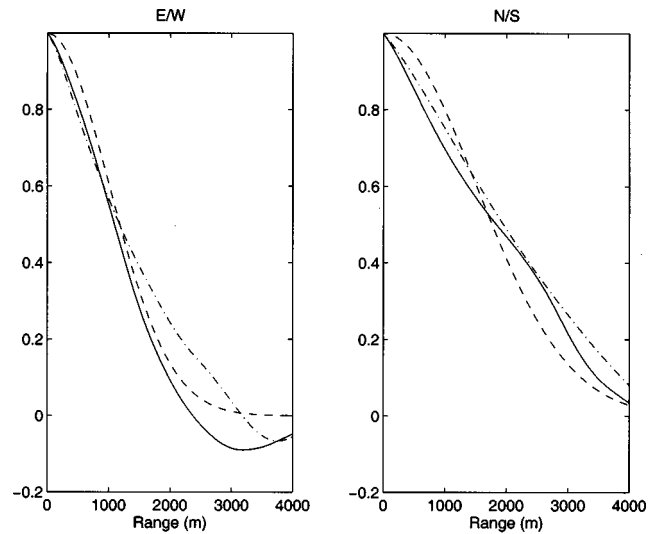


FIG. 9. Current spatial correlation function. Left panel: east/west component. Right panel: north/south component. Solid line: correlation along the east/west axis. Dash-dotted line: correlation along the north/south axis. Dashed line: modeled correlation ($L_u = 1000$ m, $L_v = 1500$ m).

lence is not properly accounted for in the tidal model and cannot be spatially resolved by the array of moorings, it will be ignored in the present analysis. The current correlation function in time is therefore fitted using the measurements made in the North/South direction in the middle of the channel, which accounts for most of the flow energy. In the absence of detailed experimental data regarding the spatial variability of the tidal flow, the current spatial correlation was estimated using the field predicted by Foreman's model (see Fig. 9). The correlation function of both flow components was assumed to be of the form¹⁹

$$\Gamma_u(\Delta x, \Delta y, \Delta t) = e^{-(1/2)R_u^2}, \quad (35)$$

where

$$R_u^2 = \left(\frac{\Delta x}{L_x}\right)^2 + \left(\frac{\Delta y}{L_y}\right)^2 + \left(\frac{\Delta t}{T_u}\right)^2.$$

The correlation lengths L_x and L_y were both set equal to 1000 m for the east/west component and 1500 m for the north/south component. The correlation time T_u was estimated to be approximately 2 h.

The sound speed correlation in depth was estimated using a set of conductivity-temperature-salinity (CTD) casts taken over the month of June 1996. Detailed experimental data of the sound speed spatial variability being scarce as well, the horizontal spatial correlation function of the sound speed field was assumed to be identical to that of the north/south component of the tidal flow. The temporal correlation function of the sound speed field was fitted using a modified Gaussian as suggested by Carter and Robinson.¹⁹ The complete correlation function of the sound speed field was assumed to be as follows:

$$\Gamma_c(\Delta x, \Delta y, \Delta z, \Delta t) = \left[1 - \left(\frac{\Delta t}{T_c}\right)^2\right] e^{-(1/2)R_c^2}, \quad (36)$$

where

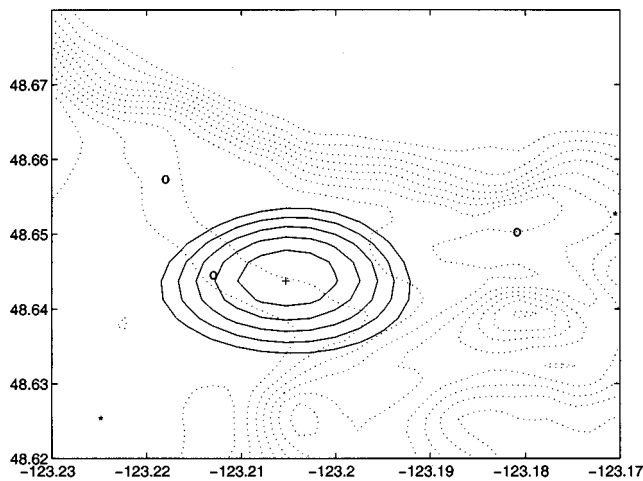


FIG. 10. Resolution kernel of the sound speed inversion. Solid lines: isokernel lines (0.5 to 1.0). Dotted lines: isobaths. Stars: IOS moorings. Circles: WHOI moorings.

$$R_c^2 = \left(\frac{\Delta x}{L_x}\right)^2 + \left(\frac{\Delta y}{L_y}\right)^2 + \left(\frac{\Delta z}{L_z}\right)^2 + \left(\frac{\Delta t}{T_c}\right)^2.$$

The correlation lengths L_x and L_y were set equal to 1500 m. The correlation depth T_z was estimated at 12 m. The correlation time T_c was estimated at 3.5 h. The difference in correlation times between the current and the sound speed correlation functions is due to variations in the functional

form used to fit to the data. The width of both main lobes is approximately the same.

Due to the periodic character of tidal forcing, the data show a relatively high degree of temporal correlation over the course of several days. However, the actual correlation level past the first 12 h is highly dependent on location and, for current, orientation of the measurement. The model correlation functions Γ_c and Γ_u were consequently constrained to vanish for lags extending beyond approximately half a day, so that a single functional form could fit a wide variety of data. Data gathered more than a few correlation lengths or times away from the estimation time were therefore not taken into account.

D. Resolution

The resolution matrix \mathbf{T} relates the field perturbation estimate \hat{x} to its true value x' .⁷ It is conveniently expressed in dimensionless form and can be thought of as the prism through which the observer perceives reality. In the ideal case \mathbf{T} is the identity matrix and the estimated quantity is equal to its true value. In practice it is rarely so. The k th column of \mathbf{T} represents the field estimate generated in response to a true field which is zero everywhere except at the k th node where it has a unit value. This response is sometimes called the resolution kernel; an example is shown in Fig. 10. The width of the resolution kernel, i.e., the resolution length, is a measure of the spatial distance over which

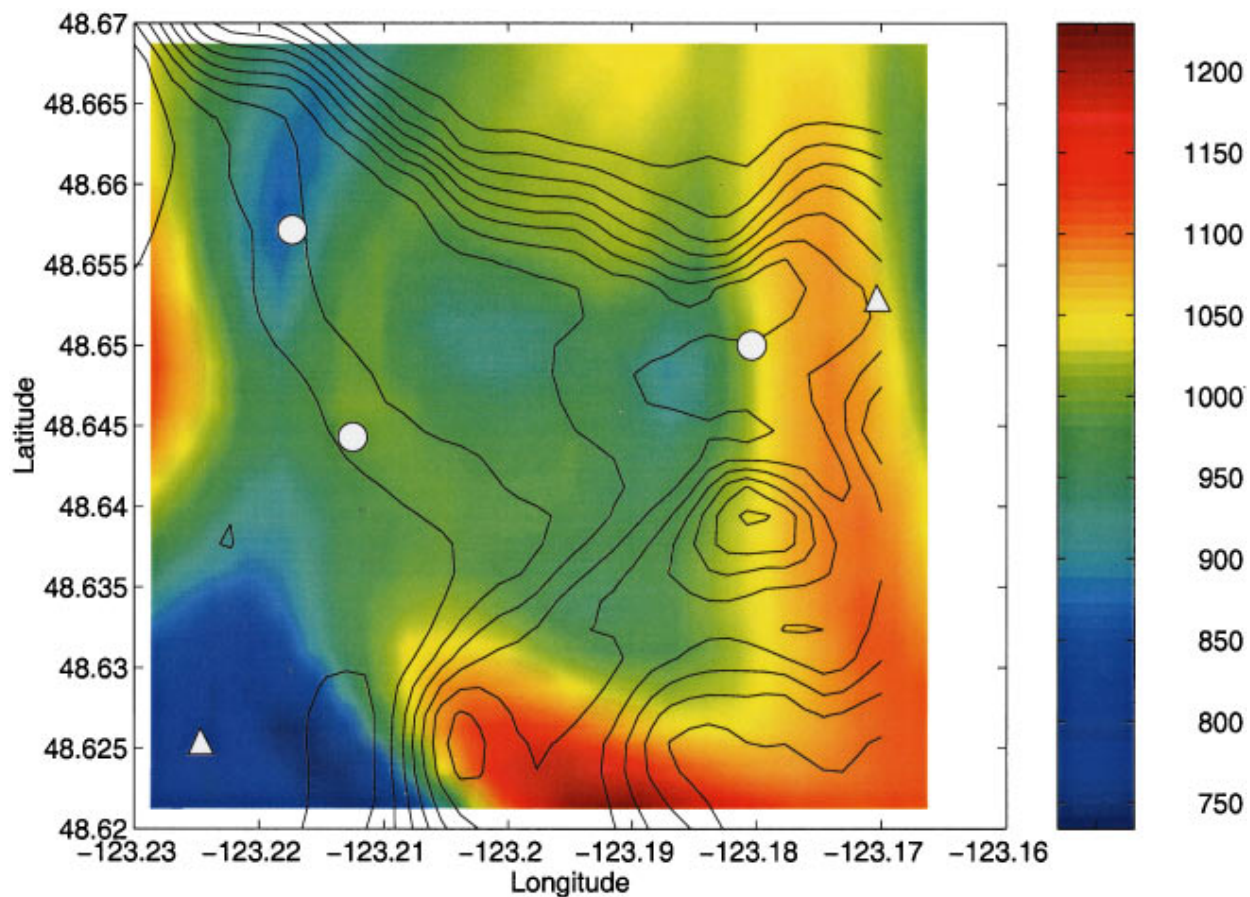


FIG. 11. East/west resolution length of the sound speed inversion. Solid lines: isobaths. Triangles: IOS moorings. Circles: WHOI moorings.

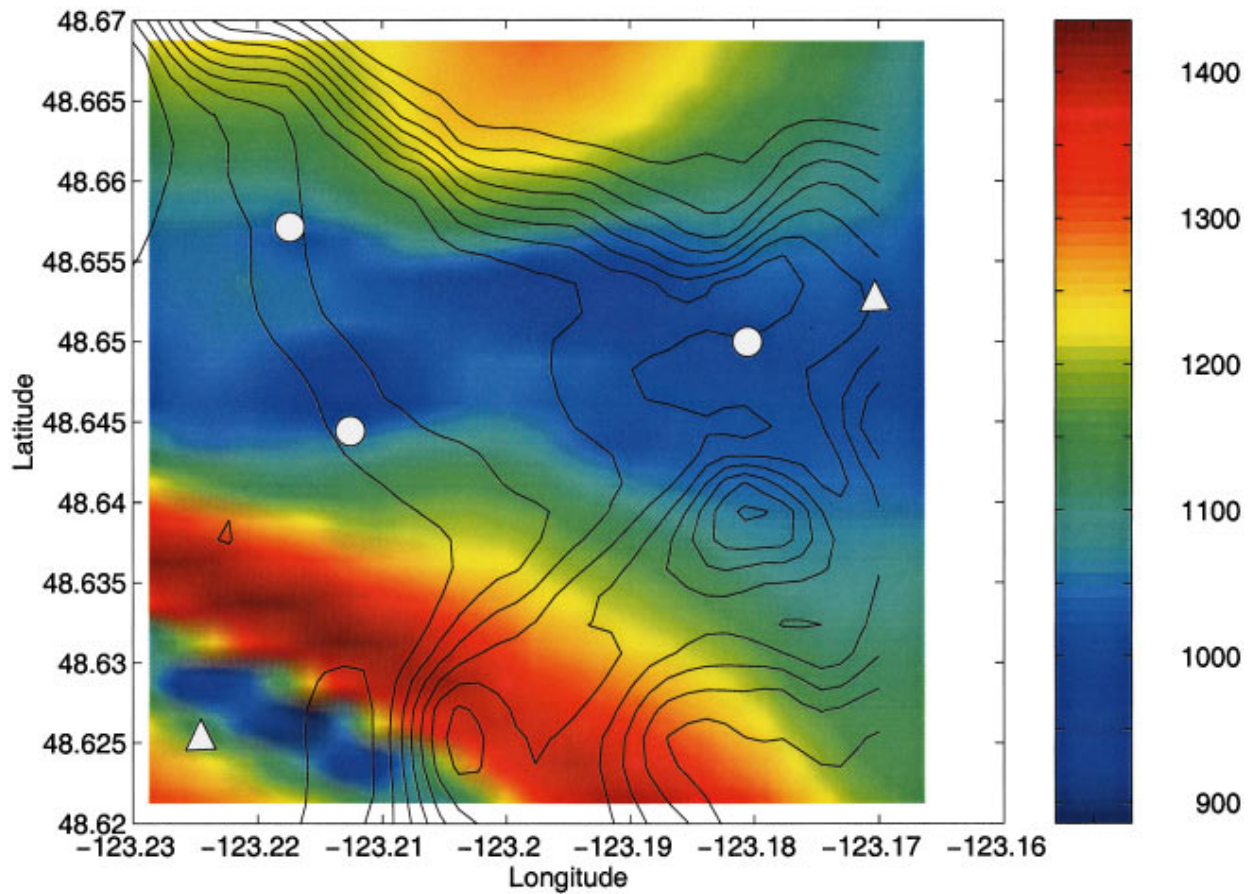


FIG. 12. North/south resolution length of the sound speed inversion. Solid lines: isobaths. Triangles: IOS moorings. Circles: WHOI moorings.

the estimate is averaged, and as such gives an indication of the level of detail the inversion procedure might be able to resolve. Various metrics can be chosen in order to compute the resolution length. Chiu suggested computing the width of the region which contains half the total energy spread by the kernel around the original true value.²⁵ However, this becomes a problem when sampling is very sparse and irregular as the resolution kernel is no longer necessarily well behaved

and energy might be unevenly spread. By interpreting the resolution kernel (or its absolute value) as a two-dimensional probability density function, one can easily compute its second moment, which will provide a measure of resolution length. In addition, an equivalent bias of the inversion can be estimated by comparing the first moment to the true location.

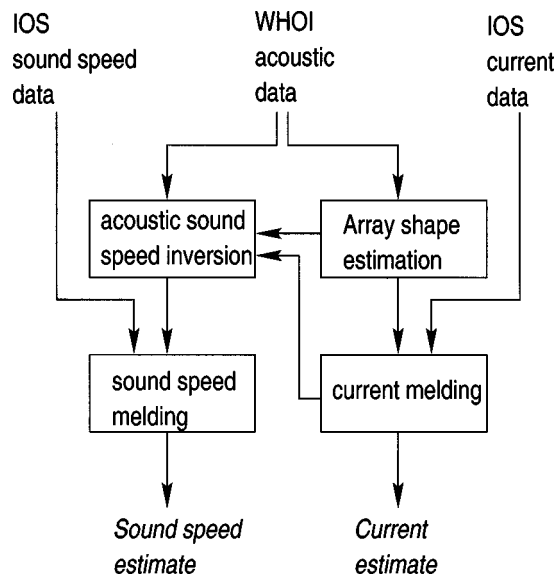


FIG. 13. Flow chart of the current and temperature field estimation scheme.

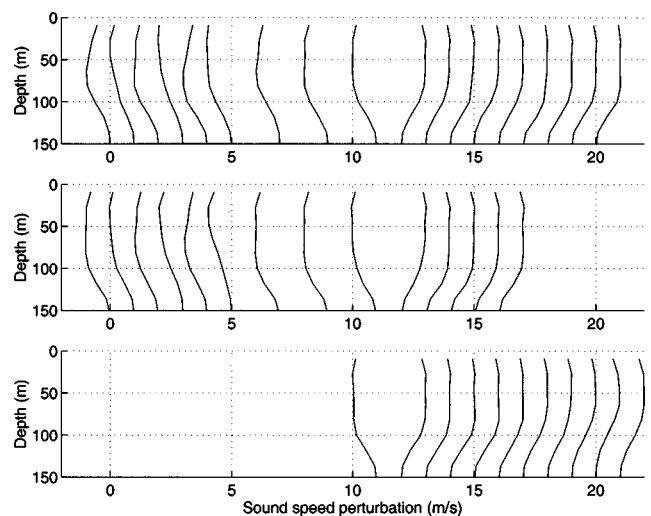


FIG. 14. Inverted acoustic sound speed profiles (synthetic data). Shots 20 to 42. Shots which were not properly captured by the acquisition system, or for which surface and direct arrivals were indistinguishable, are missing. Top panel: SW WHOI mooring. Middle panel: NW WHOI mooring. Bottom panel: NE WHOI mooring.

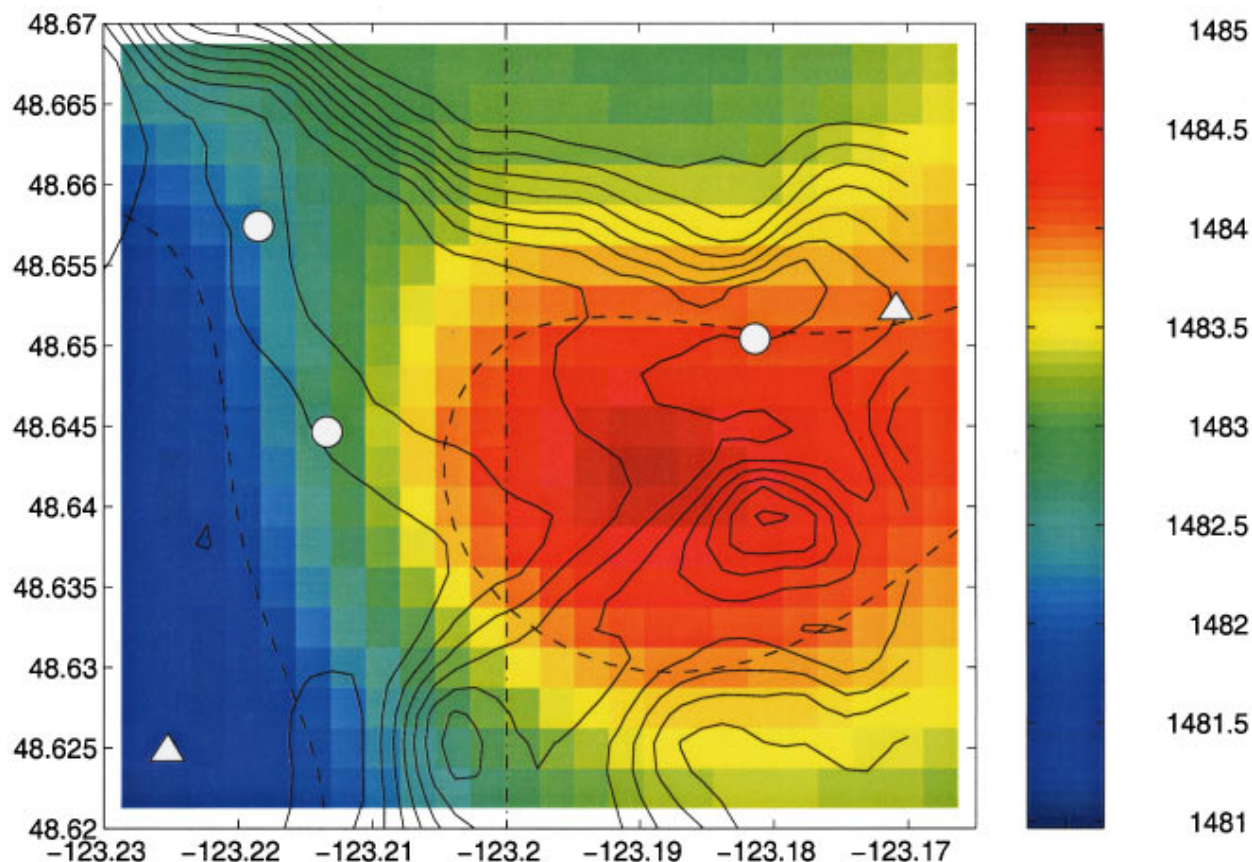


FIG. 15. Inverted sound speed field perturbation (synthetic data). Solid lines: isobaths. Dash-dotted line: actual front location. Dotted lines: isovelocity lines (1482 and 1484 m/s) Triangles: IOS moorings. Circles: WHOI moorings.

This bias is, in general, close to zero within the sampling network and starts becoming non-negligible outside the network envelope.

East/west and north/south resolution length maps are shown in Figs. 11 and 12. The east/west and north/south resolution lengths are respectively about 950 and 1000 m at the center of the network of arrays. The east/west resolution length estimate is biased near the eastern and western boundaries of the computational domains as the kernel cannot extend beyond the boundary and becomes distorted. The same effect is seen along the northern and southern boundaries for the north/south resolution length estimate. In particular, the low length region in the south-western corner is an artifact due to the proximity of the boundary combined with the experimental geometry.

E. Computational issues

A flow chart of the complete current and temperature field estimation scheme is given in Fig. 13. The acoustic sound speed profiles were first computed along each propagation track and then melded with the nonacoustic data instead of being included directly in the three-dimensional inversion for several reasons. Due to the particular experimental configuration of Haro Strait, the acoustic inversion has virtually no resolution in range for a given shot. The acoustic data provides good resolution in depth and across shot tracks. This information can be efficiently extracted by processing shots individually before the global inversion. In

addition the computational load associated with a global three-dimensional inversion is of order $O(N^6)$ for a grid of dimension N^3 . On the other hand, the segmented three-dimensional inversion is of order $O(N^5)$ if carried out depth by depth, or even $O(N^4)$ if a single depth or a few selected depths are of interest. This decrease of the computational load by one to two orders of magnitude is critical in enabling this inversion to be performed in a few minutes (on a DEC-Alpha 3000) and then fed back to the sampling network, in particular to the moving sources and AUVs. Segmenting the sound speed in this manner also facilitates inversion quality control by enabling the operator to verify the validity of the acoustically derived sound speed profiles prior to melding with other data sets. The computational load of the inversion is further decreased by clipping the data sets. Data points within three correlation depths of the desired depth and acquired during a period of three correlation times before the time of inversion are taken into account. Other data points are discarded. The current field estimation was made first. It was then used as background field in the sound speed estimation.

III. RESULTS

A. Synthetic data

In order to evaluate the accuracy of the inversion procedure a synthetic data set was generated. The simulated environment was identical to that of Haro Strait. The sound speed

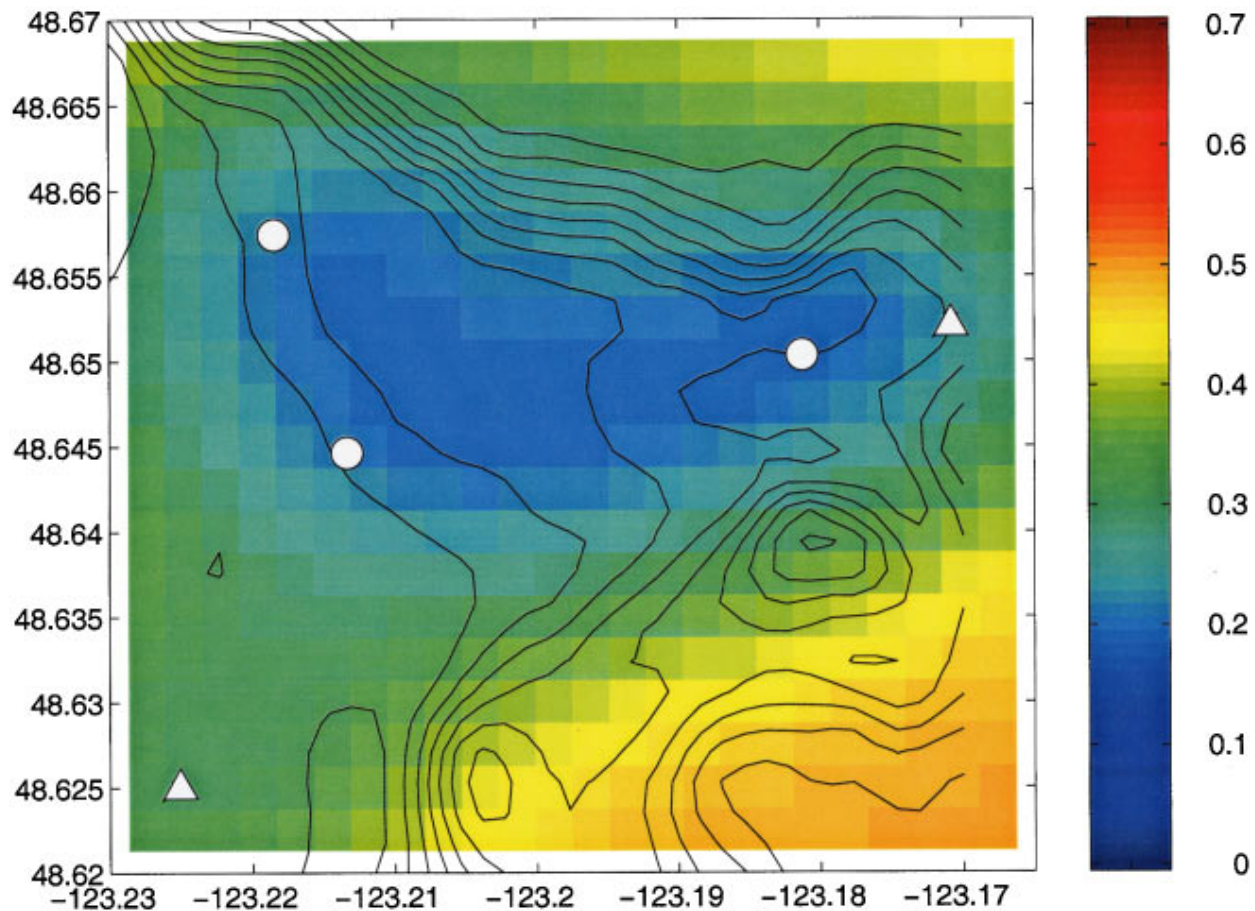


FIG. 16. Estimated error of the inverted sound speed field perturbation (synthetic data). Solid lines: isobaths. Triangles: IOS moorings. Circles: WHOI moorings.

field was assumed to be split in two isovelocity regions: the water sound speed was equal to 1484 m/s on the eastern side of the -123.20 meridian, and 1482 m/s on the western side. The transition at the meridian was set to be discontinuous, which is not physical but allows a better understanding of the resolution limits of the inversion. The environment was assumed to be steady. In the absence of cyclical tidal variations, the sound speed correlation function was assumed to be a pure Gaussian.

The sound speed profiles computed using Eq. (25) are shown in Fig. 14. Actual profiles are isovelocity. The lower half of the water column is notinsonified by the direct and surface rays and is therefore not resolved by the inversion. The surface layer is weakly resolved by the first few shots, which were fired at short range between the SW and NW WHOI moorings. Some inaccuracies are consequently observed in the corresponding sound speed profiles.

The estimated sound speed field is shown in Fig. 15. The associated error field is shown in Fig. 16. Two separate effects can be observed in Fig. 15. First the sound speed field is smeared in space due to the assumed correlation. The front is no longer a sharp discontinuity but a smooth transition zone with a width of about 1200 m, or a little less than a correlation length (1500 m). Then the front is shifted by about half a correlation length to the west of the actual front line at the latitude of maximum discrepancy. This is related to the confidence level in the acoustic data gathered between

the two westernmost WHOI moorings. Due to the short ranges of the shots fired between these two moorings, the estimated error of the acoustic sound speed profiles is high relative to those measured along longer tracks east of the SW

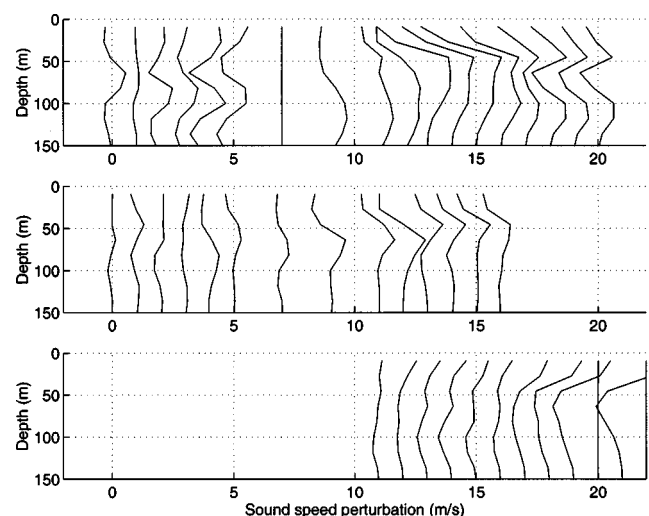


FIG. 17. Inverted acoustic sound speed profiles (Haro Strait data). Shots 20 to 42. Shots which were not properly captured by the acquisition system, or for which direct and surface arrivals were indistinguishable, are missing. Top panel: SW WHOI mooring. Middle panel: NW WHOI mooring. Bottom panel: NE WHOI mooring.

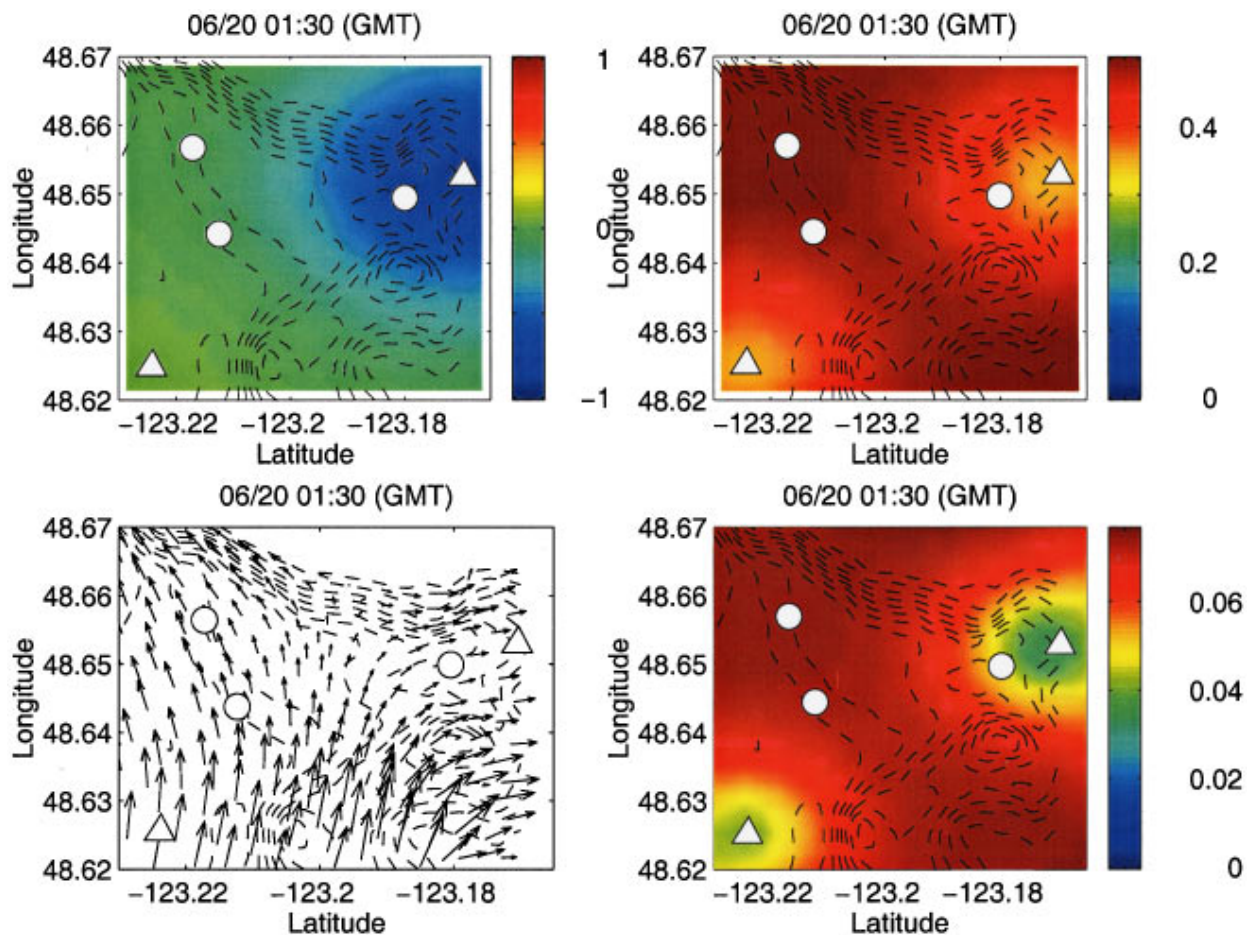


FIG. 18. Top view of the Haro Strait site at 01:30 GMT at a depth of 25 m. Upper left panel: sound speed (m/s); upper right panel: sound speed error (m/s); lower left panel: current field (m/s); lower right panel: current perturbation error prior to melding (m/s). Dashed lines: isobaths. Triangles: IOS moorings. Circles: WHOI acoustic moorings.

WHOI mooring. When the various acoustic profiles are merged with the local IOS measurements, the inverse estimate is constrained to be 1484 m/s on the east side of the -123.20 meridian with a relatively low error and 1482 m/s on the west side with a somewhat higher error level. The smoothness constraint imposed by the correlation function then shifts the estimated front position towards the region of higher uncertainty.

Tidal currents were included in the sound speed reference state. Current effects on the estimated sound speed field are most pronounced between the SW and NW WHOI moorings where the flow is strongest and parallel to the acoustic propagation track. Neglecting the current field in the inversion leads to an antisymmetric shift of the sound speed field between the SW and NW WHOI moorings, resulting in an east/west inflection of the 1483 m/s isovelocity line at this location.

B. Haro Strait data

The acoustic sound speed profiles estimated using the actual Haro Strait data set are shown in Fig. 17. The final field estimate merging integral acoustic data with local non-acoustic data is shown for three different times in Figs. 18, 19, and 20. The 01:30 GMT estimate does not yet incorporate acoustic data. The error field is consequently relatively high

except near the IOS mooring locations. The 02:30 GMT estimate includes acoustic data from the first seven shots. Those shots were fired mostly between the SW and NW WHOI moorings and a significant decrease can be observed on the sound speed error map (upper right) near the location of the shots. A local decrease can be observed on the current error map (lower right) at the location of the SW and NW WHOI moorings. This is due to the fact that acoustically derived array shape data are now assimilated in the current estimate. The 03:30 GMT estimate includes all acoustic data. The sound speed error level has been significantly lowered over the entire region surrounded by the WHOI moorings. The combination of acoustically derived array shape data at the NE WHOI mooring with data from the nearby IOS mooring leads to a sharp decrease of the current error level. Interestingly enough, this decrease is not observed at other locations where the current estimate relies on a single type of data only.

C. Discussion

The scarcity of relevant oceanographic data, particularly in coastal environments such as Haro Strait, makes it difficult to compare the field estimates described above with an independent data set. Aside from the synthetic data test discussed in Sec. III A, the actual estimates can be compared to

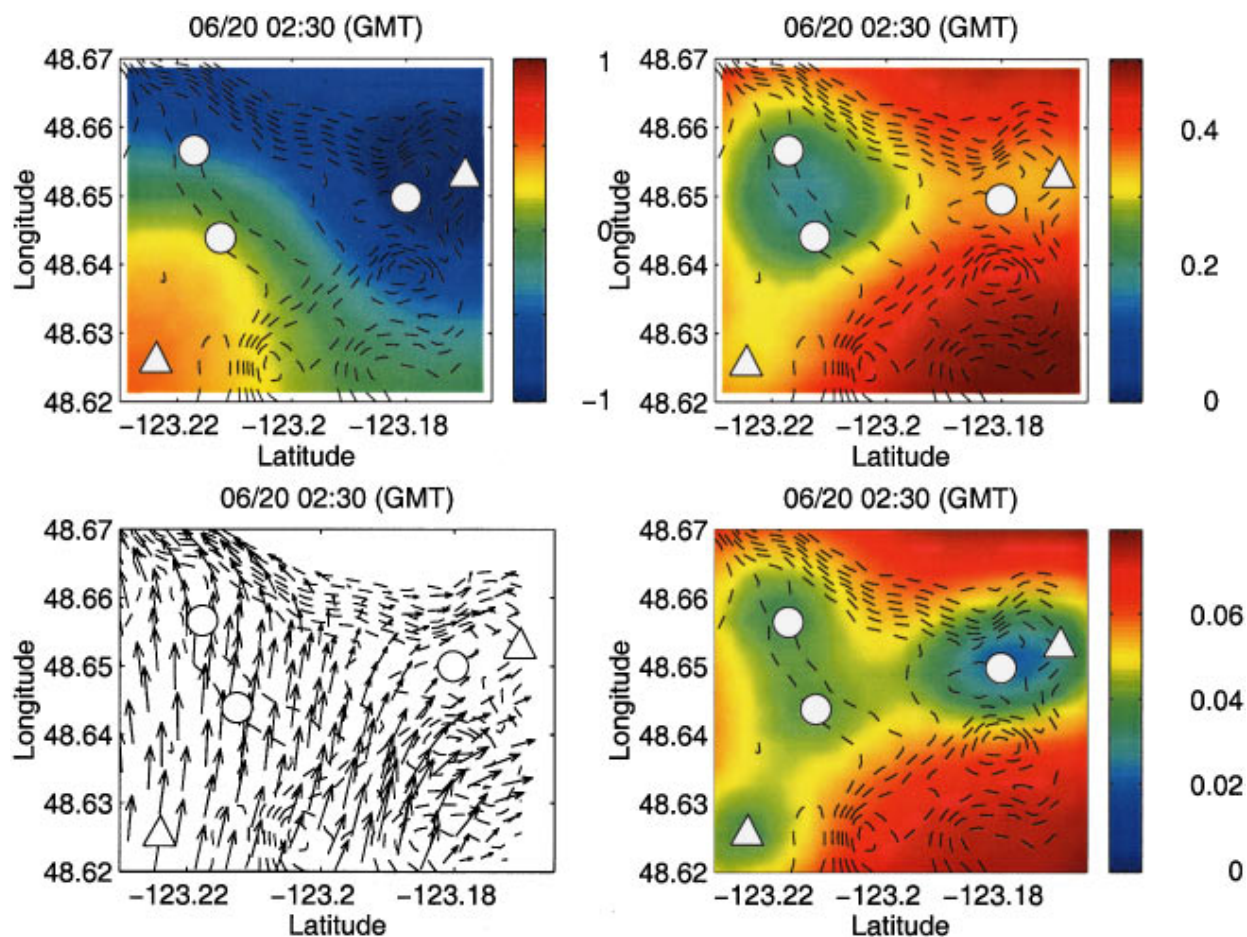


FIG. 19. Top view of the Haro Strait site at 02:30 GMT at a depth of 25 m. Upper left panel: sound speed (m/s); upper right panel: sound speed error (m/s); lower left panel: current field (m/s); lower right panel: current perturbation error prior to melding (m/s). Dashed lines: isobaths. Triangles: IOS moorings. Circles: WHOI acoustic moorings.

independent temperature records taken at the NW and NE WHOI moorings. Although no concomitant salinity measurements were performed, these temperature records can be converted into an equivalent sound speed by taking into account the strong correlation between temperature and salinity. A linear regression on a set of CTD casts taken a week after this experiment yields the following result:

$$c = 1.3043T + 1470.6, \quad (37)$$

where c is the sound speed in m/s and T is the temperature in $^{\circ}\text{C}$. The regression correlation (R^2) is 0.94. The 95% confidence intervals for the gradient and constant terms are ± 0.0233 and ± 0.22 , respectively. The resulting comparison is shown in Fig. 21. Acoustic data are assimilated from 02:00 on. The temperature being around 10°C , the error induced by the regression is approximately 0.43 m/s, which accounts for some of the 0.8 m/s bias observed in Fig. 21. The remainder is attributable to the inversion itself and possible calibration offsets between the WHOI thermistors and the IOS temperature sensors.

The combination of multiple data sets enables the inversion procedure to overcome the individual limitations these might have. The acoustic data set, for instance, is limited in its ability to measure an absolute sound speed by the fact that the source transmission time is not known accurately and

must be estimated when localizing array elements. Thanks to clock synchronization across the acoustic network, sound speed differences can still be measured across different depths and different tracks. On the other hand, the IOS mooring time series provide us with an absolute sound speed reference, but are obviously limited in coverage as shown in Fig. 18, which shows the field estimates before any acoustic data is taken into account. The acoustic array shapes by themselves are a local indication of the current magnitude, but contain almost no information regarding its direction. However, they yield a relatively low-error current estimate in magnitude and direction when combined with the IOS time series and assimilated into Foreman's tidal model. By furthermore coupling the sound speed inversion with the current inversion, the current/sound speed ambiguity inherent to any acoustic inversion can be, to some extent, resolved without resorting to reciprocal transmissions. This is made possible by extracting the information contained in different data sets through the combined inversion described in Sec. II.

Combining oceanographic with acoustic data and models traditionally brings up several issues, both theoretical and computational. The resolution of an oceanic field estimate, for instance, must match that of the acoustic model if an accurate acoustic prediction is to be made based on this field estimate and at an acceptable computational cost.²⁶ If the

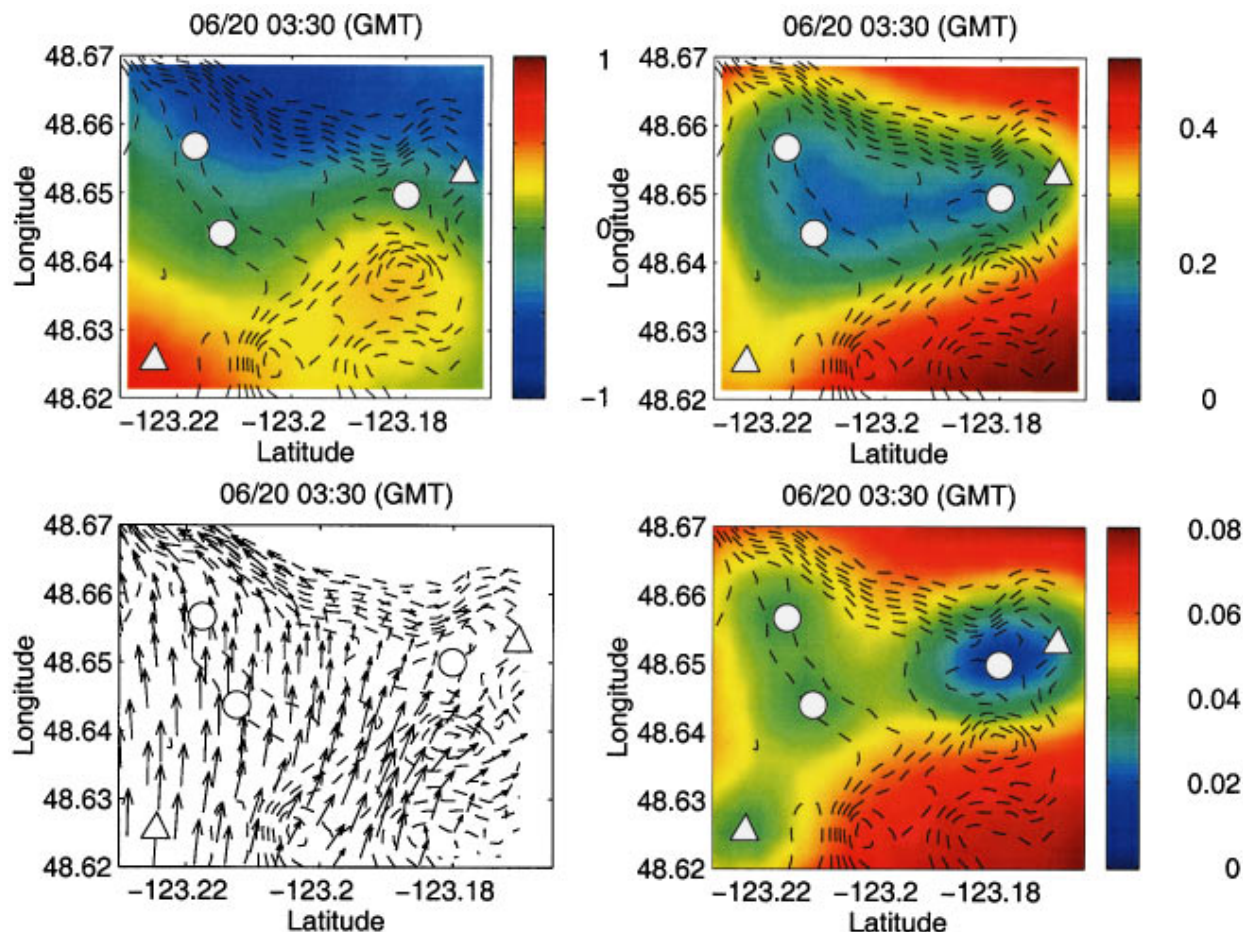


FIG. 20. Top view of the Haro Strait site at 03:30 GMT at a depth of 25 m. Upper left panel: sound speed (m/s); upper right panel: sound speed error (m/s); lower left panel: current field (m/s); lower right panel: current perturbation error prior to melding (m/s). Dashed lines: isobaths. Triangles: IOS moorings. Circles: WHOI acoustic moorings.

field estimate is itself inaccurate, the acoustic prediction might diverge widely from reality due to the nonlinear dependence of the wave equation on environmental fields. In the present analysis the current field used as input to the acoustic model is produced by a barotropic tidal model. No vertical stratification is therefore added to the reference acoustic sound speed profile. Furthermore, given the short ranges involved in the Haro Strait experiment, an individual acoustic transmission has no resolution in range and rays are sensitive primarily to the range-averaged sound-speed profile. The effect of using the tidal current field estimate as input to the ray tracer is then linear for all practical purposes. The effective sound speed profile is offset by some small constant quantity, which yields an approximately constant shift in travel times at the receiver array. The vertical variability of the current field is modeled as additional noise.

The robustness of the current melding scheme [see Eq. (22)] is ensured by the fact that data and model are melded *externally*, i.e., linearly. Of the four basic operations described in Fig. 13, three are therefore linear. The only non-linear operation is the array shape estimation, based on mean square travel time difference minimization. Due to the short ranges involved in this paper, this operation can be carried out before the actual sound speed inversion by assuming some constant sound speed profile. Were longer ranges to be

involved, the shape estimation would need to be either based on independent short-range acoustic transmissions or included in the sound speed inversion. The robustness of the overall inversion scheme derives then from its linearity, i.e., its simplicity, and the combination of different data sets with different resolutions and coverages.

Finally, it is worth noticing that, due to the particular experimental configuration adopted in Haro Strait, the final field estimate might be somewhat biased (see Sec. III A). In addition, the error estimate of the sound speed field does not formally propagate the error of the current estimate it used as its input. Error modeling, in particular in the case of oceanographic and acoustic model coupling, is still an active area of research and an accurate error model for the final field estimate lies beyond the scope of this paper. However, the error fields analyzed with the Haro Strait experiment do show the potential impact of melding different types of data and models on the resulting estimate uncertainty. The combination of various data streams and models is able to exploit the advantages of each data set, e.g., resolution or coverage, and compensate to some extent their limitations.

IV. CONCLUSION

The low-frequency acoustic data set gathered in Haro Strait in June 1996 was used in conjunction with nonacoustic

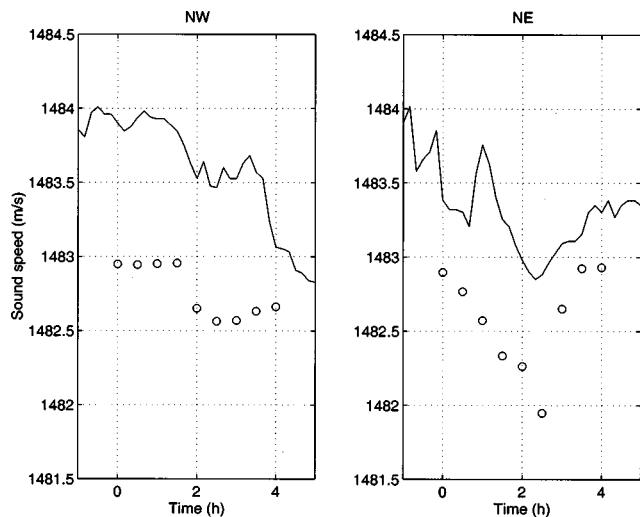


FIG. 21. Comparison with thermistor data. Left panel: NW WHOI mooring. Right panel: NE WHOI mooring. Solid line: top thermistor (approximate depth: 25 m). Dashed line: second thermistor (approximate depth: 35 m). Circles: sound speed estimate at the relevant mooring location at a depth of 25 m.

measurements in order to image a water mass of approximately 3 km by 3 km by 200 m. A fast and robust inversion algorithm combining linear techniques previously used in deep ocean tomography and oceanographic data assimilation was developed, yielding the real-time oceanic field estimates required in the context of acoustically driven rapid environmental assessment. The use of data melding and data assimilation techniques allowed us to resolve to some extent the current/sound speed ambiguity inherent to any nonreciprocal acoustic transmission. In addition, the combined use of integral and local data lead to a significant decrease of the field estimate uncertainty while maintaining a coverage of the area not achievable by nonacoustic means.

ACKNOWLEDGMENTS

The authors wish to thank the crew of the R. B. Young and the Woods Hole technicians for their invaluable help in carrying the Haro Strait experiment. Current and temperature time series were kindly provided by Kevin Bartlett (Institute of Ocean Sciences). Foreman's tidal model was run with the much appreciated help and assistance of Rich Pawlowicz (Institute of Ocean Sciences). Discussions with Carlos Lozano (Harvard University) on data assimilation helped shape the analysis presented in this paper. Finally, the authors gratefully acknowledge the reviewers' numerous comments, which contributed to making this paper significantly better than the original manuscript. Funding was provided by the Office of Naval Research through Grant No. N00014-95-1-0495.

APPENDIX: MODEL AND NOISE COVARIANCE MATRICES

1. Sound speed field

The acoustic model covariance matrix $\mathbf{R}_{cc}^{(a)}$ used in (26) was computed as

$$\mathbf{R}_{cc}^{(a)} = \sigma_c^2 \Gamma_c(\mathbf{r}_i, \mathbf{r}_j, t_i, t_j),$$

where \mathbf{r}_i refers to the location (depth) of the i th node of a given acoustic inversion (single shot, range independent). The times t_i and t_j were set equal to each other. The standard deviation σ_c was estimated to be 72 cm/s using CTD data. The acoustic noise covariance matrix $\mathbf{R}_{nn}^{(a)}$ was computed as

$$\mathbf{R}_{nn}^{(a)} = \left(\sigma_t^2 + \left(\frac{\sigma_u}{c_o} \frac{R}{c_o} \right)^2 \right) \mathbf{I},$$

where R is the source range. The first term accounts for local travel time errors. The standard deviation σ_t was set to 0.6 ms by inspection of the shots with the shortest ranges. The reference sound speed was set equal to 1500 m/s. The second term accounts for the presence of current variations in depth along the acoustic track. The current standard deviation in depth σ_u was estimated to be 38 cm/s using the current time series measured at three different depths.

The model covariance matrix $\mathbf{R}_{cc}^{(c)}$ used in the inversion of Eq. (34) was defined as

$$[\mathbf{R}_{cc}^{(c)}]_{ij} = \sigma_c^2 \Gamma_c(\mathbf{r}_i, \mathbf{r}_j, t_i, t_j),$$

where \mathbf{r}_i and t_i refer to the location in space and time of the i th node of the corresponding grid. The noise covariance matrix $\mathbf{R}_{nn}^{(u)}$ used in the inversion of (34) was computed as

$$[\mathbf{R}_{nn}^{(c)}] = \begin{bmatrix} \tilde{\sigma}_c^2 \mathbf{I} & \mathbf{O} \\ \mathbf{O} & \tilde{\mathbf{P}}_c(a) \end{bmatrix}.$$

The sound speed time series standard deviation $\tilde{\sigma}_c$ was estimated at 13 cm/s. The relevant acoustic sound speed estimate error matrices $\mathbf{P}_c^{(a)}$ given by (27) were aggregated in $\tilde{\mathbf{P}}_c^{(a)}$. Error correlations among different sound speed estimates of the same profile were therefore taken into account.

2. Current field

The model covariance matrix in (20) is defined by

$$\mathbf{R}_{uu} = E[\mathbf{u}' \mathbf{u}'^T],$$

where the first half of \mathbf{u}' includes east/west components and the second half includes north/south components. Due to the complexity and the variability of the cross correlation between the east/west and north/south components, each component was assumed to be uncorrelated with its counterpart. The model covariance matrix was therefore written as

$$\mathbf{R}_{uu} = \begin{bmatrix} \mathbf{R}_{u,x} & \mathbf{O} \\ \mathbf{O} & \mathbf{R}_{u,y} \end{bmatrix}$$

and

$$[\mathbf{R}_{u,x/y}]_{ij} = \sigma_{u,x/y}^2 \Gamma_u(\mathbf{r}_i, \mathbf{r}_j, t_i, t_j),$$

where \mathbf{r}_i and t_i refer to the location in space and time of the i th node. After comparison of the IOS current-meter data with Foreman's tidal model, the east/west standard deviation $\sigma_{u,x}$ was estimated to vary between 18 and 24 cm/s; the north/south standard deviation $\sigma_{u,y}$ was estimated to vary between 16 and 22 cm/s. Both were set to 22 cm/s in the current inversion.

Similarly, the noise covariance matrix $\mathbf{R}_{nn}^{(u)}$ was given by

$$\mathbf{R}_{nn}^{(u)} = \begin{bmatrix} \tilde{\mathbf{R}}_{u,x} & \mathbf{O} & \mathbf{R}_{au,x}^T \\ \mathbf{O} & \tilde{\mathbf{R}}_{u,y} & \mathbf{R}_{au,y}^T \\ \mathbf{R}_{au,x} & \mathbf{R}_{au,y} & \mathbf{R}_{aa} \end{bmatrix},$$

where the matrices $\tilde{\mathbf{R}}_{u,x/y}$ were computed using the definition of $\mathbf{R}_{u,x/y}$ with the actual measurement locations. The covariance of the array shape factors $\tilde{\mathbf{a}}$ with the current components $u_{x/y}$ was computed as

$$\mathbf{R}_{au,x} = \mathbf{H}_1 E[\mathbf{u}_{x,a} \mathbf{u}_x^T], \quad \mathbf{R}_{au,y} = \mathbf{H}_2 E[\mathbf{u}_{y,a} \mathbf{u}_y^T],$$

where \mathbf{H}_1 and \mathbf{H}_2 are given by (15) and (16) and the expectations by $\sigma_u^2 \Gamma_u$. For simplicity's sake the covariance of array shape factors was assumed to be

$$\mathbf{R}_{aa} = \sigma_a^2 \mathbf{I},$$

where the standard deviation σ_a was estimated at 0.02 by comparison of the array shape data with the predictions based on Foreman's model.

- ¹W. Munk and C. Wunsch, "Ocean acoustic tomography: a scheme for large scale monitoring," *Deep Sea Res.* **26A**, 123–161 (1979).
- ²D. Behringer, T. Birdsall, M. Brown, B. Cornuelle, R. Heinmiller, R. Knöz, K. Metzger, W. Munk, J. Spiesberger, R. Spindel, D. Webb, P. Worcester, and C. Wunsch, "A demonstration of ocean acoustic tomography," *Nature (London)* **299**, 121–125 (1982).
- ³B. M. Howe, "Multiple receivers in single vertical slice ocean acoustic tomography experiments," *J. Geophys. Res.* **92**(C9), 9479–9486 (1987).
- ⁴B. Cornuelle, W. Munk, and P. Worcester, "Ocean acoustic tomography from ships," *J. Geophys. Res.* **94**, 6232–6250 (1989).
- ⁵B. D. Dushaw, P. F. Worcester, B. D. Cornuelle, and B. M. Howe, "Barotropic currents and vorticity in the central north Pacific Ocean during summer 1987 determined from long-range reciprocal acoustic transmission," *J. Geophys. Res.* **99**, 3263–3272 (1994).
- ⁶R. H. Headrick, J. L. Spiesberger, and P. J. Bushong, "Tidal signals in basin-scale acoustic transmissions," *J. Acoust. Soc. Am.* **93**, 790–802 (1993).
- ⁷W. Munk, P. Worcester, and C. Wunsch, *Ocean Acoustic Tomography* (Cambridge U.P., Cambridge, 1995).
- ⁸H. A. DeFerrari and H. B. Nguyen, "Acoustic reciprocal transmission experiments, Florida Straits," *J. Acoust. Soc. Am.* **79**, 299–315 (1986).
- ⁹C. S. Chiu, J. H. Miller, and J. F. Lynch, "Inverse techniques for coastal acoustic tomography," in *Theoretical and Computational Acoustics—Volume 2*, edited by D. Lee and M. H. Schultz (World Scientific, Singapore, 1994), pp. 917–931.
- ¹⁰C. S. Chiu, J. H. Miller, W. W. Denner, and J. F. Lynch, "Forward modeling of the Barents sea tomography vertical line array data and inversion highlights," in *Full Field Inversion Methods in Ocean and Seismo-acoustics*, edited by O. Diaschok, A. Caiti, P. Gerstoft, and H. Schmidt (Kluwer Academic, Dordrecht, 1995), pp. 237–242.

- ¹¹J. F. Lynch, G. Jin, R. Pawlowicz, D. Ray, Plueddemann, C. S. Chiu, J. H. Miller, R. H. Bourke, A. R. Parsons, and R. Muench, "Acoustic travel-time perturbations due to shallow-water internal waves and internal tides in the Barents sea polar front: Theory and experiment," *J. Acoust. Soc. Am.* **99**, 803–821 (1996).
- ¹²H. Schmidt, J. G. Bellingham, and P. Elisseeff, "Acoustically Focused Oceanographic Sampling in coastal environments," in *Rapid Environmental Assessment*, edited by E. Pouliquen, A. D. Kirwan, and R. T. Pearson, Conference Proceedings Series CP-44, SACLANTCEN, 1997, pp. 145–157.
- ¹³J. G. Bellingham, H. Schmidt, and M. Deffenbaugh, "Acoustically focused oceanographic sampling in the Haro Strait experiment," *J. Acoust. Soc. Am.* **100**, 2612 (1996).
- ¹⁴D. Lee, "Three-dimensional effects: interface between the Harvard Open Ocean Model and a three-dimensional acoustic model," in *Oceanography and Acoustics: Prediction and Propagation Models*, edited by A. R. Robinson and D. Lee (AIP, New York, 1994).
- ¹⁵A. R. Robinson, J. C. Carman, and S. M. Glenn, "A dynamical system for acoustic applications," in *Oceanography and Acoustics: Prediction and Propagation Models*, edited by A. R. Robinson and D. Lee (AIP, New York, 1994), pp. 80–117.
- ¹⁶C. J. Lozano, A. R. Robinson, H. G. Arango, A. Gangopadhyay, Q. Sloan, P. J. Haley, L. Anderson, and W. Leslie, "An interdisciplinary ocean prediction system: assimilation strategies and structured data models," in *Modern Approaches to Data Assimilation in Ocean Modeling*, edited by P. Malanotte-Rizzoli (Elsevier, Amsterdam, 1996), pp. 413–452.
- ¹⁷M. Grund, M. Johnson, and D. Herold, "Haro Strait tidal front mapping experiment," Technical report, Woods Hole Oceanographic Institution, February 1997.
- ¹⁸K. V. Mackenzie, "Nine-term equation for sound speed in the oceans," *J. Acoust. Soc. Am.* **70**, 807–812 (1981).
- ¹⁹E. F. Carter and A. R. Robinson, "Analysis models for the estimation of oceanic fields," *J. Atmos. Ocean. Technol.* **4**, 49–74 (1987).
- ²⁰T. K. Kapoor, "Three-dimensional acoustic scattering from arctic ice protuberances," Ph.D. thesis, Massachusetts Institute of Technology, June 1995.
- ²¹M. G. Foreman, R. A. Walters, R. F. Henry, C. P. Keller, and A. G. Dolling, "A tidal model for eastern Juan de Fuca Strait and the southern Strait of Georgia," *J. Geophys. Res.* **100**(C1), 721–740 (1995).
- ²²A. Tarantola, *Inverse Problem Theory—Methods for Data Fitting and Model Parameter Estimation* (Elsevier, Amsterdam, 1987).
- ²³P. Malanotte-Rizzoli, editor, *Modern Approaches to Data Assimilation in Ocean Modeling* (Elsevier, Amsterdam, 1996).
- ²⁴B. D. Cornuelle and P. F. Worcester, "Ocean acoustic tomography: integral data and ocean models," in *Modern Approaches to Data Assimilation in Ocean Modeling*, edited by P. Malanotte-Rizzoli (Elsevier, Amsterdam, 1996), pp. 97–115.
- ²⁵C. S. Chiu, J. F. Lynch, and O. M. Johanessen, "Tomographic resolution of mesoscale eddies in the Marginal Ice Zone: a preliminary study," *J. Geophys. Res.* **92**(C7), 6886–6902 (1987).
- ²⁶W. L. Siegmund, D. Lee, G. Botseas, A. R. Robinson, and S. M. Glenn, "Sensitivity issues for interfacing mesoscale ocean prediction and parabolic acoustic propagation models," in *Oceanography and Acoustics: Prediction and Propagation Models*, edited by A. R. Robinson and D. Lee (AIP, New York, 1994), pp. 133–160.